Acta Materialia 309 (2026) 122100

Contents lists available at ScienceDirect

Acta Materialia

journal homepage: www.elsevier.com/locate/actamat

Full length article

Composition-dependent electronic hybridization induced transitions in metallic glasses

Fujun Lan [a,b,c,1], Ziliang Yin [a,1], Hongbo Lou [a,b,*], Xin Zhang [a], Lianghua Xiong [d], Di Peng [a,b], Dazhe Xu [a], Chenjie Lou [a], Tao Liang [a], Mingxue Tang [a,e], Hongwei Sheng [f], Zhidan Zeng [a,b], Qiaoshi Zeng [a,b,*]

[a] Center for High Pressure Science and Technology Advanced Research (HPSTAR), Shanghai 201203, PR China
[b] Shanghai Key Laboratory of Material Frontiers Research in Extreme Environments (MFree), Shanghai Advanced Research in Physical Sciences (SHARPS), Shanghai 201203, PR China
[c] Shanghai Institute of Laser Plasma, China Academy of Engineering Physics, Shanghai 201800, PR China
[d] Shanghai Key Laboratory of Advanced High-temperature Materials and Precision Forming, School of Materials Science and Engineering, Shanghai Jiao Tong University, Shanghai 200240, PR China
[e] College of Materials Science and Engineering, University of Science and Technology Beijing, Beijing 100083, PR China
[f] Department of Physics and Astronomy, George Mason University, Fairfax, VA 22030, USA

ARTICLE INFO

Keywords:
Metallic glass
Composition-property relationships
Composition-dependence
Electronic hybridization

ABSTRACT

Metallic glasses (MGs), free from strict stoichiometry constraints, usually exhibit far greater compositional flexibility than their crystalline intermetallic counterparts. Based on a simplified picture, a near-linear or monotonic dependence of some properties on composition is often assumed and experimentally observed over a relatively broad composition range in MGs, seemingly following the rule of mixtures. The deviation from this simple compositional trend is also common in MGs, which is critical to understanding the complexity of glasses. Here, we uncover an abrupt transition in the compositional dependence of properties in the $Ce_{65}Al_{35-x}Co_x$ (at.%, $5 \leq x \leq 30$) MGs at a critical composition $x = 17.5$. The transition is consistently detected by a set of complementary experimental techniques, including synchrotron x-ray diffraction, *in situ* high/low-temperature electric resistance measurements, differential scanning calorimetry, and nanoindentation tests. This unusual transition suggests complex, composition-dependent interactions among constituent elements in MGs. Synchrotron x-ray absorption spectroscopy and nuclear magnetic resonance spectroscopy further reveal a crossover in 4*f* electron states and bonding characteristics as x varies. These findings highlight the critical roles of composition-dependent electronic structures and chemical interactions, beyond the classical random hard-sphere model, in dictating the physical properties of MGs, providing new insight into the elusive composition-structure-property relationships and guiding the design of MGs with tailored properties.

1. Introduction

Composition is a critical parameter that governs phase formation and stability in materials. In crystalline binary or multi-component compounds, varying the content of a component can, once solubility limits are exceeded, induce transitions between phases with distinct structures and properties. In other words, deviations from stoichiometric ratios destabilize existing phases while promoting alternative crystalline configurations. For example, chemical doping, which is a common strategy to induce quantum phase transitions, is often constrained by limited stoichiometric tolerance and crystalline symmetry requirements [1]. In contrast, owing to the lack of strict constraints of structural symmetry, charge neutrality, and bond angles, metallic glasses (MGs) [2] feature non-directional metallic bonds and thus possess a vast compositional space for glass formation, offering high flexibility for composition tuning and providing a unique system for fundamental studies of glasses [3]. In addition, MGs exhibit exceptional properties, such as high mechanical strength, hardness, fracture toughness, excellent

* Corresponding authors.
E-mail addresses: hongbo.lou@hpstar.ac.cn (H. Lou), zengqs@hpstar.ac.cn (Q. Zeng).
[1] These authors contribute equally to this work.

https://doi.org/10.1016/j.actamat.2026.122100
Received 28 September 2025; Received in revised form 13 February 2026; Accepted 9 March 2026
Available online 10 March 2026

wear/corrosion resistance, and good soft-magnetic properties [4–9]. Therefore, MGs have been attracting great interest in both fundamental research and industrial applications over the last decades [2,10]. While some properties of MGs often exhibit approximately linear or monotonic compositional dependences in a relatively broad composition window, consistent with the "rule of mixtures" [11], non-linear composition effects on the glass-forming ability (GFA) have remained elusive for decades [12,13]. Beyond the simple "rule of mixtures", complex chemical interactions were proposed to account for the non-linear composition effects on GFA in multiple-component MGs with metalloid elements [14] or between transition metals and post-transition metals [15], which suggest a non-negligible role of electronic structures and orbital hybridization in multi-component MGs.

Recent studies have demonstrated that pressure can induce first-order-like polyamorphic transitions in MGs containing elements prone to undergoing electronic transitions under compression [14–23]. For instance, in Ce-based and other rare-earth-based MGs with localized 4*f* electrons, delocalization of 4*f* electrons occurs within a relatively narrow pressure range, leading to bond-length contraction and atomic volume collapse, resulting in the transition from low-density amorphous to high-density amorphous states during compression [14–21]. Pressure has also been shown to induce devitrification in MGs, primarily attributed to electronic transitions, thereby revealing hidden long-range order within amorphous systems [24,25]. With increasing temperature, MGs undergo various structural transitions upon heating, such as glass transitions and crystallization, and, in certain systems, even glass-to-glass transitions or liquid-liquid phase transitions (LLPTs) [26–34]. Notably, unlike the rich transitions induced by pressure or temperature, composition, as another fundamental parameter, has not been reported to cause sharp transitions in MGs and is often assumed to follow a simple linear behavior based on the "rule of mixtures".

Despite the development of thousands of MGs with diverse compositions, the compositional dependence of structure and properties remains poorly understood, rendering MG development an inefficient trial-and-error process [35]. Nonetheless, pressure- or temperature-induced polyamorphic transitions in MGs exhibit compositional sensitivity, with transition pressures varying across systems [17,18] and some transitions restricted to specific compositional ranges [22,24,25,29,30]. Since transition metal elements can have a strong interaction with the 4*f* electrons and affect their electron configuration in the well-studied Ce-Co and Ce-Ni MGs [38], Ce-based MGs doped with transition metal elements could serve as ideal model systems to investigate whether compositional variation alone could directly induce sharp transitions in MGs. Such discoveries could bring new insights into our understanding of compositional effects in MGs by establishing a definite relationship between composition-dependent electronic structures and glass structures/properties.

Ce-Al binary MGs are a prototypical system exhibiting pressure-induced polyamorphic transitions [14,16]. In this work, we focus on the effects of transition-metal doping on Ce-Al MGs by substituting Al with Co in $Ce_{65}Al_{35-x}Co_x$ (at.%) alloys, which offer a wide glass-forming composition range [36]. This system, therefore, provides an ideal platform to probe the interplay among composition, structure, and properties while enabling electronic structure modulation. Using a combination of multiple structural and property characterization techniques, we reveal two distinct glass states with a sharp transition at around $x = 17.5$, confirming an unusual composition-induced sharp transition in MGs.

2. Experimental details

2.1. Sample preparation

Eleven master ingots with nominal compositions of $Ce_{65}Al_{35-x}Co_x$ (at.%, $5 \leq x \leq 30$, with an increment of 2.5%) were prepared by arc-melting using high-purity Ce (99.9 at.%), Co (99.999 at.%), and Al (99.999 at.%) under a titanium-gettered high-purity argon atmosphere. Each ingot was flipped and remelted five times, with electromagnetic stirring applied during the first two cycles, to ensure chemical homogeneity. Then, MG ribbons (with a thickness of ~20 μm and a width of ~1.2 mm) were obtained via the single-roller melt-spinning method under high-purity argon with a copper wheel speed of ~40 m/s and a melt temperature of ~1323 K, which maintains nearly identical effective cooling rates and thermal histories for all ribbon samples.

2.2. X-ray diffraction measurements

X-ray diffraction (XRD) experiments were performed at the beamline 15U1 of Shanghai Synchrotron Radiation Facility (SSRF), China, with an x-ray wavelength of 0.6199 Å and a focused beam size of ~3 × 4 μm^2. Two-dimensional (2D) diffraction images were collected using an SX165 CCD detector with a 10 s exposure time per sample. These 2D images were subsequently integrated into one-dimensional $I(q)$ patterns using the Dioptas software [37].

2.3. Differential scanning calorimetry measurements

The thermodynamic properties of all $Ce_{65}Al_{35-x}Co_x$ samples were characterized by differential scanning calorimetry (DSC, Perkin-Elmer DSC8500) with a constant heating rate of 20 K/min and an argon flow rate of 30 mL/min. The activation energy values of glass transition and crystallization of the samples were obtained from DSC measurements performed at heating rates of 5, 10, 20, 40, and 80 K/min. The annealed samples refer to those heated to the center temperature of their first exothermic peak (above the glass transition temperature) at a rate of 20 K/min, followed by immediate cooling to room temperature at a rate of 50 K/min.

2.4. Aberration-corrected transmission electron microscopy measurements

The amorphous structural features at the nanoscale of a representative composition with $x > 17.5$, $Ce_{65}Al_{10}Co_{25}$, in both as-prepared and annealed (at the first exothermic peak) states were investigated using aberration-corrected transmission electron microscopy (TEM). High-resolution TEM (HRTEM) images and selected area electron diffraction (SAED) patterns were acquired on a ThermoFisher Spectra 300 transmission electron microscope equipped with dual spherical aberration correctors. The two TEM specimens were prepared using a focused ion beam system (FEI, Versa 3D).

2.5. Mechanical properties measurements

The mechanical properties of all $Ce_{65}Al_{35-x}Co_x$ samples were evaluated via load-displacement (*P-h*) curves using the instrumented nanoindentation (Agilent Nano Indenter G200) with a standard Berkovich diamond indenter. All nanoindentation tests were performed in the load control mode with a loading rate of 0.05 mN/s and a maximum load of 15 mN. Six indentations per sample were performed to determine the average hardness and modulus using the Oliver-Pharr method [38].

2.6. In situ high/low-temperature resistance measurements

The *in situ* high-temperature resistance measurements were performed using a Linkam HFS600E-PB4 probe stage under a high-purity argon atmosphere, with temperatures ranging from 303 K to 380 K at a heating rate of 20 K/min. The resistance values were measured using the standard four-probe method, employing a direct current (DC) source (Keithley 6221) to supply a constant current and a nanovoltmeter (Keithley 2182A) to monitor the voltage. *In situ* low-temperature resistance measurements were performed from 2 K to 300 K using a Physical Property Measurement System (PPMS-9T, Quantum Design), employing

the four-probe method with DC.

2.7. Ce L_3-edge x-ray absorption spectroscopy measurements

The Ce L_3-edge x-ray absorption spectroscopy (XAS) experiments were performed on the as-prepared $Ce_{65}Al_{35-x}Co_x$ MG samples (x = 5, 10, 17.5, 25, and 30) using the transmission mode at the beamline 13-IDE of Advanced Photon Source (APS), Argonne National Laboratory (ANL). Each sample was polished to ~7 μm in thickness prior to XAS experiments.

2.8. Nuclear magnetic resonance spectroscopy measurements

The solid-state ^{27}Al nuclear magnetic resonance (NMR) spectra of the as-prepared $Ce_{65}Al_{35-x}Co_x$ samples were acquired with an NMR spectrometer (Bruker AVANCE NEO 600 MHz) at 14.1 T and room temperature using a 3.2 mm HXY magic-angle-spinning (MAS) probe. The ^{27}Al Larmor frequency was determined to be 156.66 MHz. All ^{27}Al NMR spectra were acquired with solid-echo pulse sequences under static conditions, referenced to $Al(NO_3)_3$ (0 ppm) and calibrated against AlF_3 powder (-17 ppm). A π/2 pulse duration of 4.5 μs and a recycle delay of 300 ms were employed. The isotropic Knight shift (K_{iso}) corresponds to the peak position of the central lines of ^{27}Al NMR spectra.

3. Results

3.1. Thermal properties of the $Ce_{65}Al_{35-x}Co_x$ MG samples

Fig. 1a presents synchrotron XRD patterns of all as-prepared $Ce_{65}Al_{35-x}Co_x$ MG samples, confirming their fully amorphous nature without any detectable sharp Bragg peaks. The features indicating continuous and systematic structural changes are clearly observable in the XRD patterns with increasing Co content, including the disappearance of the pre peak near ~1.6 Å^{-1}, the progressive broadening of the first main peak near ~2.3 Å^{-1}, and the sharpening of the second peak near ~3.9 Å^{-1}. Upon heating, glasses, as a metastable system, typically undergo pronounced structural relaxation through the glass transition, followed by progressive destabilization toward stable crystalline phases. These thermal responses constitute intrinsic "fingerprints" of the specific glass. Fig. 1b shows the DSC curves characterizing their thermal behaviors, which exhibit multiple exothermic peaks above the glass transition temperature (T_g). Here, for clarity, we denote T_c as the center temperature of the first exothermic peak following T_g. To study the thermodynamic process corresponding to the first exothermic peak,

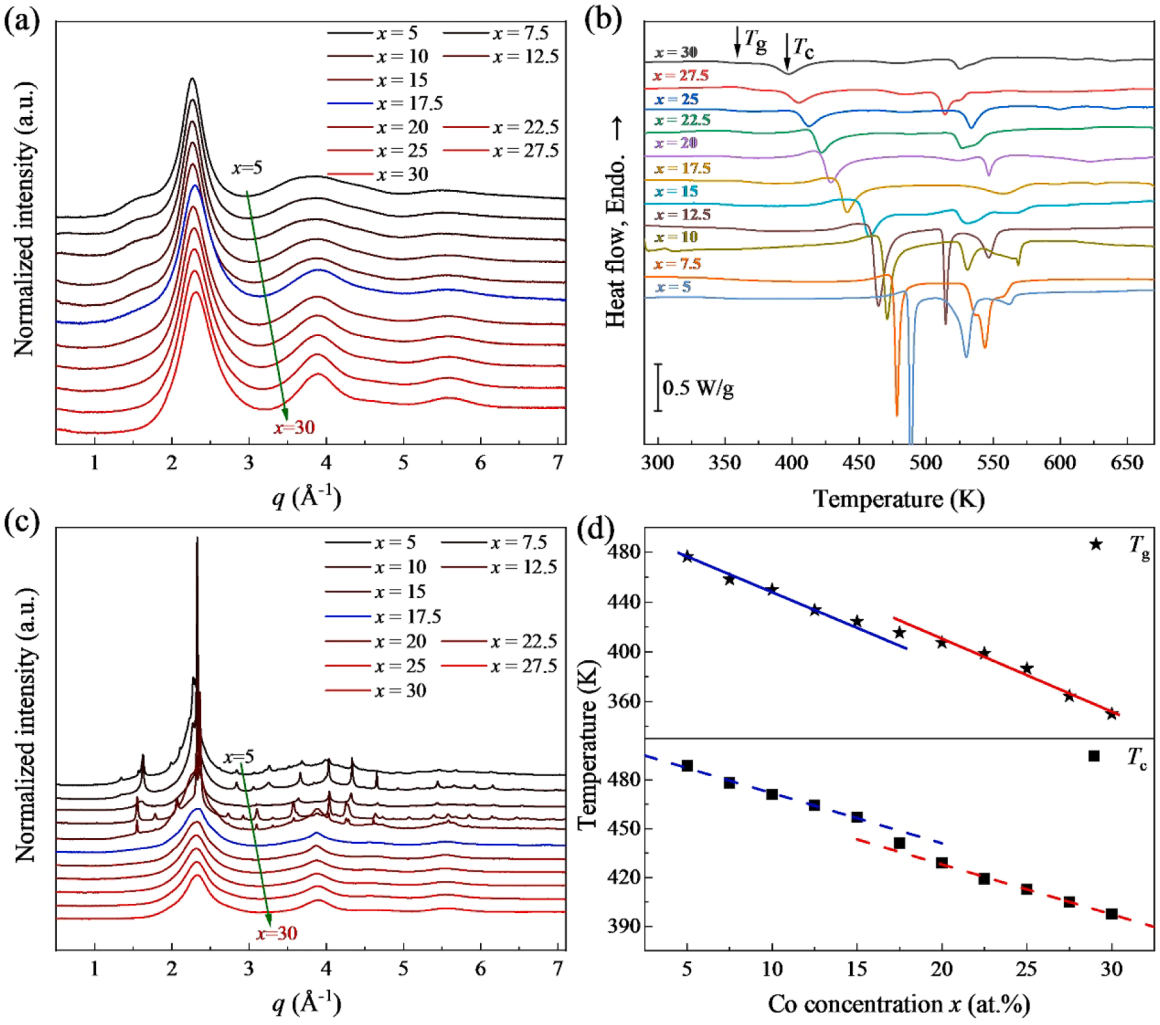

Fig. 1. XRD patterns and thermal analysis of $Ce_{65}Al_{35-x}Co_x$ MG samples. (a) Synchrotron XRD patterns of as-prepared $Ce_{65}Al_{35-x}Co_x$ MG samples. (b) DSC curves (mass-normalized) of as-prepared MG samples at a heating rate of 20 K/min. (c) Synchrotron XRD patterns of annealed samples, prepared by heating as-prepared samples to T_c at 20 K/min, followed by immediate quenching to room temperature at 50 K/min. (d) The T_g (upper panel) and T_c (lower panel) of as-prepared MG samples as a function of Co content. The red and blue lines are guides to the eye, which are not intended to show a sharp step-like transition between two linear-like composition trends. The error bars are smaller than the symbol sizes.

annealing experiments were performed at T_c. The structure of the annealed samples was then characterized by synchrotron XRD. As shown in Fig. 1c, the annealed samples with a Co content $x < 17.5$ develop crystalline domains within an amorphous matrix, whereas those with $x > 17.5$ remain fully amorphous. To further exclude the possibility of nanocrystallization or nanoscale phase separation in the $x > 17.5$ regime, we performed additional aberration-corrected TEM characterization on a representative composition, $Ce_{65}Al_{10}Co_{25}$. As shown in Fig. S1, both the as-prepared sample and the sample annealed at T_c exhibit characteristic amorphous contrast in HRTEM images, without identifiable lattice fringes or sharp Bragg diffraction peaks in the corresponding SAED patterns. These observations provide direct microscopic evidence that the transformation occurring above T_c for $x > 17.5$ does not originate from nanocrystallization or phase separation. Prior studies indicate that MGs undergoing LLPTs or ordering in supercooled liquids (SCLs) retain amorphous structures, and quenched products maintain their glassy state [29–31]. Consequently, this implies that the first exothermic peak for $x < 17.5$ corresponds to the crystallization process of MG samples, while for $x > 17.5$, it likely signifies an LLPT or an ordering process. A more detailed structural comparison between the as-prepared sample and the sample after annealing at T_c for compositions with $x > 17.5$ can be found in our prior work for the representative $Ce_{65}Al_{10}Co_{25}$ MG [31]. Fig. 1d shows the T_g and T_c as functions of Co content (x) in $Ce_{65}Al_{35-x}Co_x$ MG samples. Both T_g and T_c decrease with increasing Co content, following two nearly parallel linear trends separated by a transitional region centered at $x = 17.5$, clearly marking a composition-dependent transition pathway.

The activation energy for a process in MGs defines the barrier controlling its kinetics, shedding light on the thermodynamic stability of the glass and its resistance to structural change. To probe the glass transition and the first exothermic peak in $Ce_{65}Al_{35-x}Co_x$ MG samples, we calculated the activation energies for the two processes at T_g and T_c using the Kissinger equation [39,40], $\ln\frac{\varphi}{T^2} \propto \frac{E}{RT}$, where φ is the heating rate, R is the gas constant, T and E are the characteristic temperature and the activation energy, respectively. Linear Kissinger regressions of $\ln(\varphi/T^2)$ versus $1/T$ across heating rates of the two processes at T_g and T_c of all MG samples are shown in Fig. 2a and b, respectively, and the corresponding activation energies, E_g and E_c, are calculated (see Table 1 for detailed information). Fig. 2c shows the E_g and E_c as functions of Co

Table 1
The activation energies E_g and E_c, and the fragility parameter m of as-prepared $Ce_{65}Al_{35-x}Co_x$ MG samples.

x (at. %)	E_g (kJ/mol)	E_c (kJ/mol)	m
5	305.9 ± 7.5	216.0 ± 8.3	33.5 ± 0.8
10	280.9 ± 5.5	183.0 ± 6.8	32.6 ± 0.6
15	251.8 ± 22.2	166.2 ± 20.1	31.0 ± 2.7
17.5	219.3 ± 18.3	169.7 ± 10.7	27.6 ± 2.3
20	186.3 ± 9.6	161.9 ± 4.1	23.9 ± 1.2
25	138.7 ± 8.1	204.4 ± 10.7	18.7 ± 1.1
30	110.1 ± 7.8	213.5 ± 12.1	16.4 ± 1.2

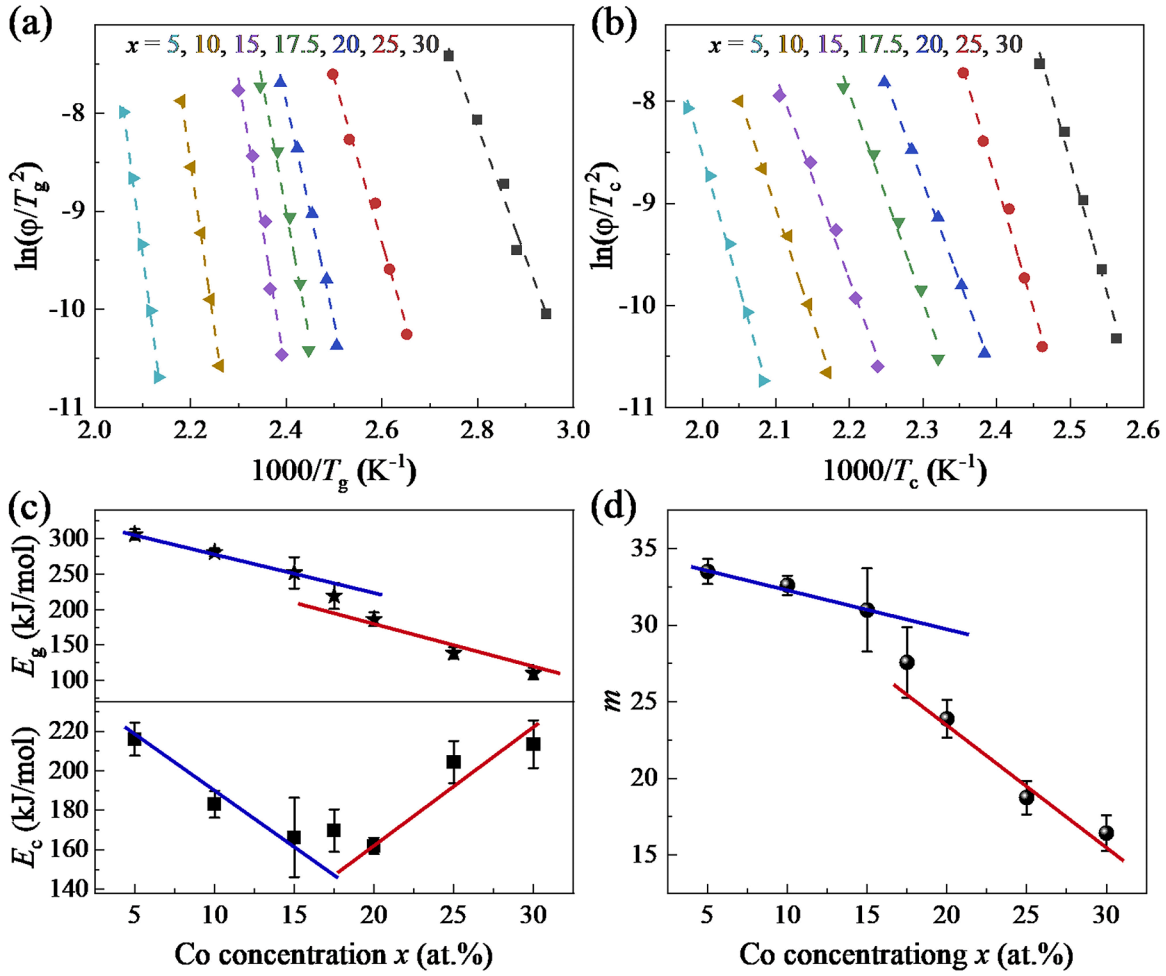

Fig. 2. The activation energy and fragility parameter m of the as-prepared $Ce_{65}Al_{35-x}Co_x$ MG samples. Kissinger analysis plots of (a) T_g and (b) T_c thermal processes as functions of heating rate. (c) Activation energies of T_g (upper panel) and T_c (lower panel) processes as a function of Co content. (d) Fragility parameter m as a function of Co content. The solid lines in (c) and (d) serve as visual guides.

content. As the Co content increases, the activation energy of the glass transition, E_g, decreases, indicating reduced thermal stability, consistent with the observed decline in T_g. Again, within this overall downward trend, a distinct transition is evident at $x = 17.5$. By contrast, E_c exhibits a non-monotonic dependence: it first decreases and then increases with x, showing a critical point at $x = 17.5$. This transition is attributed to two distinct kinetic processes occurring at T_c in the low- and high-Co MG samples: crystallization dominates in the low-Co content region, whereas LLPTs (ordering) likely occur at T_c in the high-Co content region. These results elucidate that $Ce_{65}Al_{35-x}Co_x$ MG samples can be divided into two categories of distinct MGs exhibiting fundamentally different thermodynamic behaviors. Furthermore, the fragility parameter m, calculated by $m = \frac{E_g}{ln10RT_g}$ [41–43], decrease from 33.5 to 16.4 as Co replaces Al, as shown in Fig. 2d and Table 1. Following the definition of Angell [44], this decline indicates the viscous flow of $Ce_{65}Al_{35-x}Co_x$ MG samples changes into a much stronger behavior as Co content increases. Thus, both activation energy trends and fragility parameters consistently indicate a composition-induced transition in $Ce_{65}Al_{35-x}Co_x$ MG samples.

3.2. Mechanical properties of the $Ce_{65}Al_{35-x}Co_x$ MG samples

Fig. 3a shows the *P-h* curves of all $Ce_{65}Al_{35-x}Co_x$ MG samples in nanoindentation measurements. To enhance clarity, curves are parallelly offset with only loading portions displayed except for the $Ce_{65}Al_5Co_{30}$ sample, where an unloading curve is included. The inset of Fig. 3a provides a closer look at the intermittent discontinuities typically termed as "pop-in" events [45–47]. It is apparent that low-Co MG samples ($x < 17.5$) exhibit pronounced "pop-ins", whereas high-Co MG samples ($x > 17.5$) show smooth *P-h* curves. The "pop-in" events usually reflect the intermittent plastic yielding in MGs, corresponding to the nucleation and propagation of shear bands, which are widely observed in MGs [45–50]. Their occurrence usually depends on the ductility and chemical composition of MGs, often signaling transitions of plastic deformation modes [48–51]. Therefore, these results imply that with an increase in the Co content, the $Ce_{65}Al_{35-x}Co_x$ MG samples undergo a transition from discontinuous to relatively continuous plastic deformation under mechanical loading. The hardness of MGs, obtained from the *P-h* curves, decreases systematically with the increasing Co content, but with a slope change around $x = 17.5$, as shown in Fig. 3b.

3.3. Electrical transport properties of the $Ce_{65}Al_{35-x}Co_x$ MG samples

Electrical resistance is a highly sensitive probe for detecting structural variations in MGs [52–56]. *In situ* high-temperature resistance measurements were performed on as-prepared $Ce_{65}Al_{35-x}Co_x$ MG samples to assess the effect of composition on electrical transport properties. Fig. 4a displays the relative resistance $R_T/R_{303\ K}$ versus temperature of

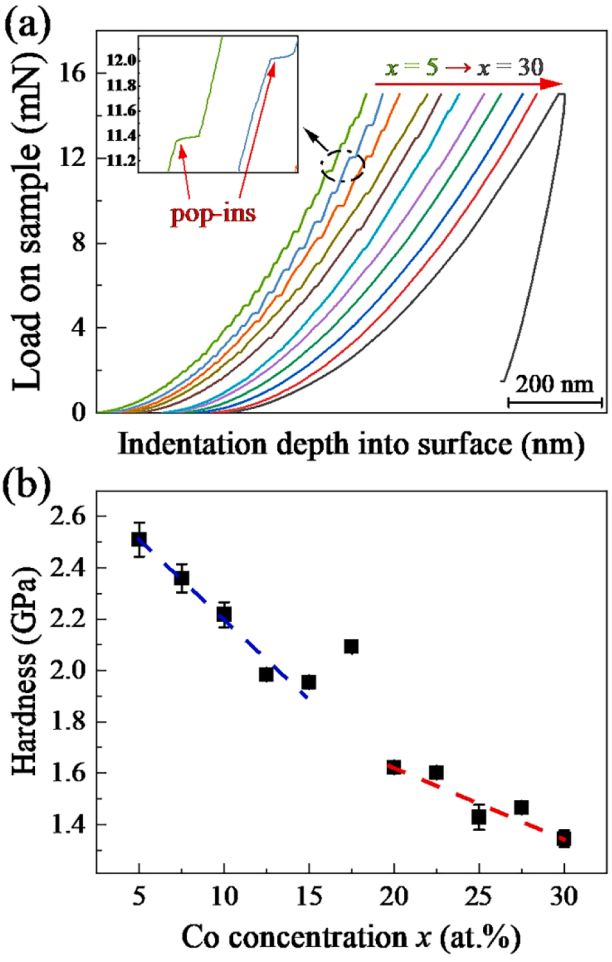

Fig. 3. Nanoindentation analysis of the as-prepared $Ce_{65}Al_{35-x}Co_x$ MG samples. (a) *P-h* curves from nanoindentation experiments (loading portion) of as-prepared MG samples. All nanoindentation tests were performed in the load control mode with a maximum load of 15 mN and a loading rate of 0.05 mN/s. Curves are parallelly offset for clarity, with the inset highlighting the "pop-ins" events. (b) Hardness of the as-prepared MG samples as a function of Co content. The solid lines serve as visual guides.

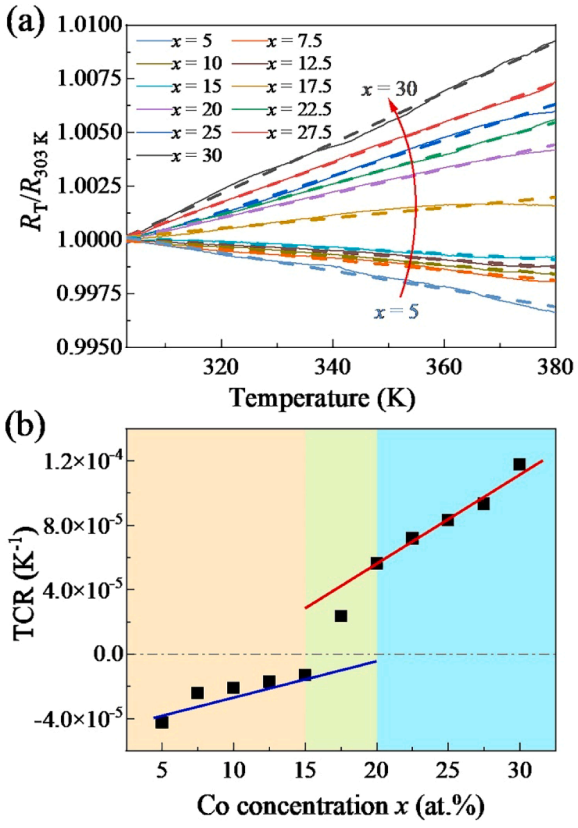

Fig. 4. Electrical transport properties of the as-prepared $Ce_{65}Al_{35-x}Co_x$ MG samples. (a) The relative resistance $R_T/R_{303\ K}$ of the as-prepared MG samples as a function of temperature. Solid lines represent experimental data, while dashed lines denote linear fits to the resistance in the temperature range from 303 K to 373 K. (b) The TCR of the as-prepared MG samples as a function of Co content. Solid lines serve as visual guides, and the error bars are smaller than symbol sizes.

all $Ce_{65}Al_{35-x}Co_x$ MG samples, where R_T and $R_{303\ K}$ denote the resistance at temperatures T and 303 K, respectively. Solid lines represent experimental data, which exhibit near-linear behavior below the T_g despite minor fluctuations from thermal/contact-related artifacts. The temperature coefficient of resistance (TCR) was determined by linear fitting between 303 and 373 K (dashed lines).

As shown in Fig. 4b, the low-Co MG samples ($x < 17.5$) exhibit negative TCR, whereas high-Co MG samples ($x > 17.5$) display positive TCR. According to previous studies, MGs with positive TCR are generally consistent with the near-free electron model, while negative TCR is typically associated with localized electronic states or hybridization between *sp*- and *d*-orbitals [57–60]. These findings suggest that composition variation induces a transition in the electrical transport properties in $Ce_{65}Al_{35-x}Co_x$ MG samples, which is likely attributed to changes in the electronic structure.

3.4. Electronic structures of $Ce_{65}Al_{35-x}Co_x$ MG samples

In-situ low-temperature resistance measurements were carried out to investigate the Ce 4*f* electron states in $Ce_{65}Al_{35-x}Co_x$ MG samples as a function of composition. As shown in Figs. 5a and b, in the low-temperature region below 50 K, the relative resistance $R_T/R_{300\ K}$ of low-Co MG samples exhibits a minimum near ~8 K, and follows a negative log T dependence below ~8 K. Both are characteristic features of the Kondo effect, as previously observed in some Ce-based crystalline materials [61] and MGs [62]. The resistance minima weaken progressively with the increasing Co content and completely disappear when $x > 20$. Furthermore, the minima shift toward lower temperatures as Co content increases, suggesting reduced magnetic scattering from the localized 4*f* electrons of Ce. These findings suggest that increasing Co content gradually suppresses the Kondo effect: low-Co MG samples show a gradually weakening Kondo effect, while high-Co MG samples lack measurable Kondo behavior. Since the Kondo effect arises from interactions between conduction electrons and localized 4*f* moments, its suppression implies a progressive delocalization of Ce 4*f* electrons with increasing Co content. This electronic transition correlates well with the observed compositional boundary that divides $Ce_{65}Al_{35-x}Co_x$ MG samples into two distinct groups. In addition, as shown in Fig. 5a, the low-Co MG samples show an increasing negative TCR above 50 K, which is consistent with the trends observed in the high-temperature resistance measurements. Furthermore, the speculation of the relationship between the 4*f* electron delocalization and composition of $Ce_{65}Al_{35-x}Co_x$ MG samples was clarified using Ce L_3-edge XAS experiments, as shown in Fig. 6. When $x = 5$, the spectrum shows only a $4f^1$ component, indicating a fully localized 4*f* electron configuration. With increasing Co content, a post-edge feature corresponding to a delocalized $4f^0$ state emerges at ~10 eV above the $4f^1$ peak [16,63], and its intensity increases at the expense of the $4f^1$ component's intensity. This spectral evolution reflects the valence state shifts, where higher Co concentrations redistribute the spectral weight from localized $4f^1$ to delocalized $4f^0$ states, as reported in Ce-bearing crystalline materials [63–66] and Ce-based MGs [16], providing direct experimental evidence that the composition regulation does lead to major changes in the electronic structure of $Ce_{65}Al_{35-x}Co_x$ MG samples.

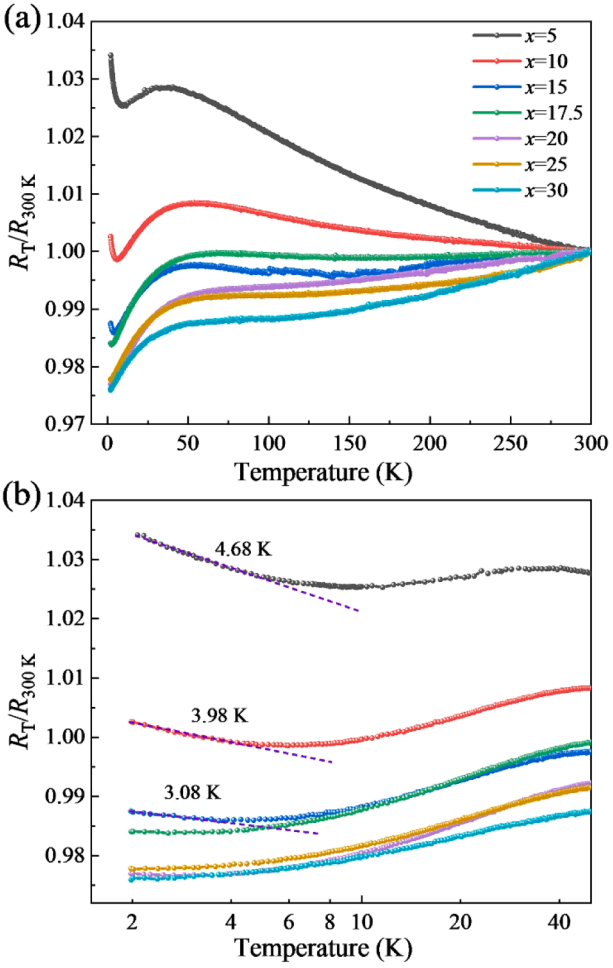

Fig. 5. The low-temperature resistance of the as-prepared $Ce_{65}Al_{35-x}Co_x$ MG samples. (a) The relative resistance $R_T/R_{300\ K}$ of as-prepared MG samples as a function of temperature from 2 K to 300 K. (b) The logarithmic temperature dependence of relative resistance of as-prepared MG samples from 2 K to 50 K, highlighting the minima shift toward lower temperatures as Co content increases. Data were collected during heating cycles using PPMS except the sample with $x = 5$ (cooling cycle data) because of transient electrical-contact instability during its heating cycle.

4. Discussion

Achieving continuous tuning of material properties over wide ranges through compositional doping is highly desirable in materials science but is often hindered by strict stoichiometric constraints or limited solubility in crystalline materials. In contrast, MGs benefit from disorder and metastability, which could greatly expand their accessible compositional space and, for certain properties, can sometimes lead to approximately linear compositional dependences within a relatively wide composition window, consistent with "rule of mixtures" descriptions. In this work, by systematically investigating compositions

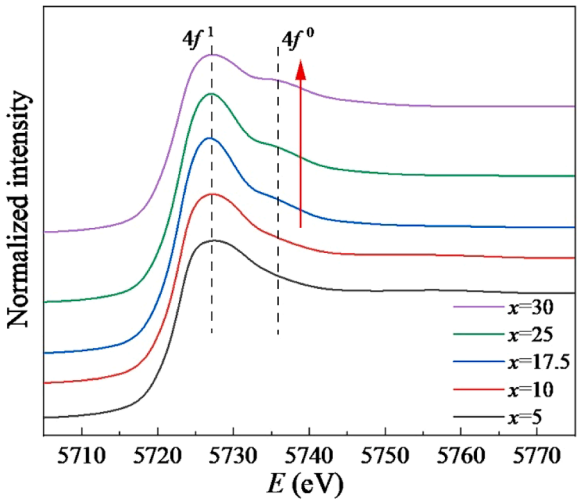

Fig. 6. The Ce L_3-edge XAS spectra of the as-prepared $Ce_{65}Al_{35-x}Co_x$ MG samples. The dashed lines highlight the positions of the $4f^0$ and $4f^1$ components.

with varying Al:Co ratios in the $Ce_{65}Al_{35-x}Co_x$ MG system, we provide comprehensive experimental evidence of a sharp transition separating two distinct regimes.

Ce and Ce-based intermetallics have attracted considerable attention owing to their rich polymorphic transitions and attractive physical properties, which are intrinsically derived from the strong electronic correlations between Ce-4*f* electrons and their hybridization with valence electrons [67–69]. The chemical environment of Ce atoms, which is governed by their neighboring atoms, determines whether 4*f* electrons will remain localized, hybridize with delocalized valence states, or occupy intermediate configurations. In Ce-bearing systems, 4*f* electrons frequently escape localization but remain incompletely delocalized, forming an "intermediate-valence" or a "mixed-valence" state [63,65,70]. This behavior originates from the near-degeneracy of localized $4f^1$ and delocalized $4f^0$ configurations, facilitated by shallow 4*f* energy levels close to the Fermi surface. Even weak hybridization could destabilize the localized 4*f* electrons, driving their delocalization. In our previous work, the Ce-Al binary MGs were shown to exhibit pressure-induced polyamorphic transitions at relatively low pressures, which were attributed to the delocalization of Ce 4*f* electrons under pressure, confirming that this mechanism persists in amorphous materials [16]. In the present study, rather than applying external pressure, we introduce transition metal Co into the binary system to probe potential electronic hybridization effects in the Ce-Al-Co ternary system under ambient conditions.

In the $Ce_{65}Al_{35-x}Co_x$ MG system, the atomic interactions primarily involve Ce-Al, Ce-Co, and Al-Co pairs, where only the first two pairs involve 4*f* electrons. In Ce-Al binary MGs, such as $Ce_{55}Al_{45}$ [14], $Ce_{75}Al_{25}$ [16], and $Ce_{89}Al_{11}$ [71], although the delocalization of 4*f* electrons occurs under pressure and leads to polyamorphic transitions, the 4*f* electrons remain fully localized under ambient conditions, even in solute-lean systems like $Al_{93}Ce_7$ [21]. These results indicate that the Ce-Al pair cannot drive 4*f*-electron delocalization. In contrast, Ce-Co binary systems were reported to exhibit pronounced 4*f*-electron delocalization. For example, the amorphous $Ce_{75.5}Co_{24.5}$ alloy exhibits significant delocalization of the Ce 4*f* shell, as evidenced by its magnetic, thermal, and transport properties [70]. Maltere *et al.* [63] also found that the degree of 4*f* electron delocalization increases with increasing Co content in amorphous Ce-Co alloys. Such a delocalization behavior is also observed in crystalline Ce-Co alloys and other Ce-transition-metal systems (e.g., Ce-Ni and Ce-Fe), arising from the strong hybridization between the 3*d* orbitals of transition metals and the Ce-4*f*/5*d* orbitals [63,65–67]. Consequently, in the present $Ce_{65}Al_{35-x}Co_x$ MG system, where the Ce content is kept constant, an increase in Co content (i.e., an increase in the Ce-Co pair) is anticipated to promote electronic hybridization between Co 3*d* orbitals and Ce 4*f*/5*d* orbitals, inducing delocalization of the Ce 4*f* electrons. This is consistently demonstrated by the progressive suppression of the Kondo effect (Fig. 5) and the gradual growth of the $4f^0$ XAS peak (Fig. 6).

However, in addition to the 4*f* electron effects, many MGs exhibit complex atomic structures characterized by coexisting covalent and predominant metallic bonds [72], as was reported in systems such as $Pd_{40}Ni_{40}P_{20}$ MG [73] and some Ce-bearing MGs [74,75]. Metallic bonding primarily arises from the electrostatic interactions between a delocalized "sea" of electrons and a lattice of metal cations. In contrast, covalent bonding typically involves localized electron sharing between specific atoms, and the strength of metallic bonding depends on the valence electron concentration. In the $Ce_{65}Al_{35-x}Co_x$ system, as the Co content increases, hybridization between Co 3*d*-orbitals and Ce 4*f*/5*d*-orbitals induces a redistribution of localized Ce 4*f* electrons into the valence orbitals (5*d*6*s*). This elevates the valence electron density, thereby enhancing metallic bonding and reducing the covalent-like interactions. Moreover, as also reported in Er-Gd-Y-Al-Co high-entropy MGs, rare earth (RE)-Al clusters exhibit complex preferential covalent bonding [76]. Although the Ce-Al bonds typically exhibit metallic character, the directional hybridization of Ce's localized 4*f* orbitals with Al's *sp* electrons can foster covalent tendencies [77]. Thus, in $Ce_{65}Al_{35-x}Co_x$ MG samples, increased Co concentration could strengthen metallic bonds via orbital hybridization while diminishing covalent-like interactions.

Covalent bonds, which are generally much stronger than metallic bonds, lead to an increase in the T_g of chalcogenide glass [78]. In MG systems, decreased covalent bonding characteristics are believed to reduce the population of strongly bonded clusters, thereby lowering the activation barrier for structural rearrangement and decreasing T_g [79–81]. Thus, in the $Ce_{65}Al_{35-x}Co_x$ MG system, both T_g and E_g decrease with increasing Co content (i.e., increasing metallicity), as shown in Figs. 1d and 2c. These trends can also be qualitatively understood through the mixing enthalpy differences, where the Ce-Al, Al-Co, and Ce-Co atomic pairs exhibit mixing enthalpies of -38 kJ/mol, -19 kJ/mol, and -18 kJ/mol, respectively [82]. The non-monotonic trend in E_c (Fig. 2c) arises from competing LLPT (ordering) and crystallization processes during the first exothermic peak, as shown in Fig. 1c. Furthermore, covalent bonds enhance rigidity and shear resistance. In contrast, non-directional metallic bonds promote flexibility and deformability, which makes MGs with relatively higher covalent bonds generally exhibit higher fragility and hardness [80,81,83–86]. Therefore, as the Co content increases, the $Ce_{65}Al_{35-x}Co_x$ MG samples show a transition from discontinuous to continuous plastic deformation and a lowering hardness (Fig. 3), with fragility parameter m decreasing (Fig. 2d). For the hardness peak observed at $x = 17.5$, we confirm that this feature is reproducible with small statistical variation. Although a definitive microscopic explanation remains challenging and requires future investigation, we note that the high local stress introduced during nanoindentation may perturb the delicate electronic/bonding properties near the critical composition.

NMR spectroscopy is a powerful tool for probing electron/band states near the Fermi level of MGs [87]. Notably, ^{27}Al NMR spectroscopy has been well established as an atomic probe for characterizing covalent interactions in MGs and high-entropy alloys [88–93]. To validate the proposed hybridization-induced transition between covalent and metallic bonding in $Ce_{65}Al_{35-x}Co_x$ MG samples, ^{27}Al NMR analysis was performed on the as-prepared samples. As shown in Fig. 7, the ^{27}Al K_{iso} increases with increasing Co content. In NMR spectroscopy, an increase in K_{iso} typically correlates with a reduction in hybridized covalent-like/directional bonds in the system [92]. This indicates that substituting Co for Al progressively weakens covalent interactions. Consequently, the low-Co MG samples exhibit pronounced covalent character, whereas the high-Co MG samples possess more significant metallic bonding characteristics.

It is worth noting that the K_{iso} increment accelerates when Co concentration exceeds 17.5% in Fig. 7b. This anomaly raises a critical question: what drives the abrupt structural and property transitions consistently observed at $x = 17.5$? While the roles of Ce-Al and Ce-Co pairs have been discussed, the interaction between the Al-Co pair in the $Ce_{65}Al_{35-x}Co_x$ system remains unaddressed. Previous studies report robust hybridization between the *d*-orbitals of transition metals (Co, Ni, Cu, Ti) and the *sp*-orbitals of Al [94–98], resulting in oriented Al-transition-metal covalent bonds that enhance the fragility and hardness of MGs [76,89,90,99,100]. In the $Ce_{65}Al_{35-x}Co_x$ MG samples, as Co progressively substitutes Al from $x = 5$, the strengthening *sp*-*d* hybridization between Al and Co promotes the formation of Al-Co covalent-like bonds. The concentration of these bonds intensifies with rising Co content, reaching a maximum when Al and Co concentrations become equimolar at $x = 17.5$. Consequently, even as the Ce-Al covalent interactions decline and Ce-Co metallic bonding increases with higher Co concentrations, the increase in Al-Co covalent bonds partially compensates for the net reduction in overall covalent character. This compensatory effect is maximized in the $Ce_{65}Al_{17.5}Co_{17.5}$ composition. A further increase in Co content beyond this point reduces this covalent compensation, thereby accelerating the system's shift toward metallicity, as directly evidenced by the accelerated K_{iso} shifts in Fig. 7b.

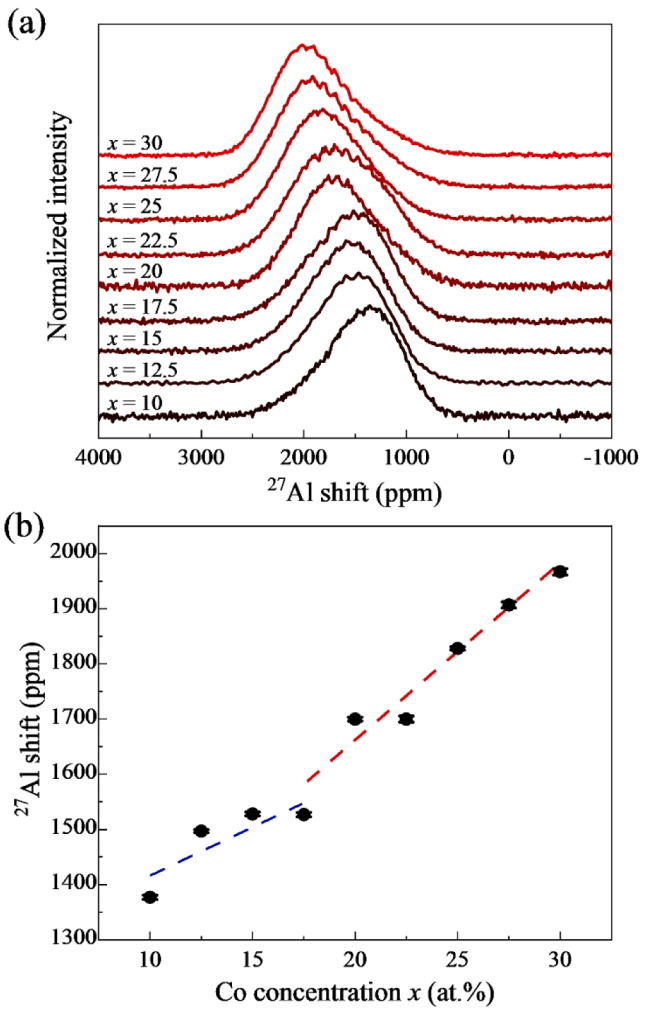

Fig. 7. NMR analysis of the as-prepared $Ce_{65}Al_{35-x}Co_x$ MG samples ($7.5 \leq x \leq 27.5$). (a) The central lines of ^{27}Al NMR spectra of $Ce_{65}Al_{35-x}Co_x$ MG samples. (b) ^{27}Al K_{iso} as a function of Co content. The dashed lines serve as visual guides.

Furthermore, the transition from a negative to a positive TCR with increasing Co content (Fig. 4b) reflects the underlying change in bonding nature, where a positive TCR is a hallmark of typical metallic behavior. This electronic hybridization-induced transition in bonding character is likely the fundamental mechanism responsible for the divergent behavior, i.e., crystallization *vs.* LLPT (ordering), observed upon annealing at T_c in the low-Co and high-Co alloys, respectively. Therefore, through comprehensive analysis, we experimentally demonstrate that continuous compositional tuning in multi-component MGs can indeed achieve dramatic and continuous property modulation. It should be emphasized that the covalent-metallic bonding balance discussed here serves as a physically motivated and internally consistent framework to interpret the observed transition-like behavior. While this framework successfully captures the experimental observations across multiple probes, the underlying composition–property relationship in highly disordered systems is inherently complex and may involve additional microscopic mechanisms beyond the present model. A more comprehensive understanding would require advanced electronic-structure-based simulations. Such approaches could further elucidate the evolution of chemical short-range order (CSRO) and provide a more complete picture of the composition-dependent transition. However, reliable simulations remain challenging at present due to the difficulty in accurately determining the Ce^{3+}/Ce^{4+} ratio for each composition as a necessary input parameter. However, beyond that, the hybridization-induced transition between covalent-like and metallic-like bonding states in the $Ce_{65}Al_{35-x}Co_x$ MG system establishes an effective strategy for controlling phase transitions in amorphous materials through electronic structure engineering.

5. Conclusions

In summary, $Ce_{65}Al_{35-x}Co_x$ MG samples, with a constant Ce content but systematically varied Co content from 5 to 30 at.% in 2.5 at.% increments, were comprehensively investigated using synchrotron XRD, DSC, *in situ* high/low-temperature resistance measurements, nanoindentation, Ce L_3-edge XAS, and ^{27}Al NMR spectroscopy. We identified a hybridization-induced transition under compositional modulation, which drives the system from a low-Co, more covalent-like regime to a high-Co, more metallic-like regime. Consequently, the $Ce_{65}Al_{35-x}Co_x$ MGs can be divided into two distinct categories, defined by abrupt differences in electronic structure, electrical transport, mechanical response, thermal stability, and bonding characteristics. This work demonstrates the first observation of an abrupt, composition-driven transition in an MG system. These findings highlight the profound role of bonding nature in amorphous materials, advance the understanding of composition-structure-property relationships, and provide guidance for designing high-performance MGs through targeted electronic-structure engineering.

CRediT authorship contribution statement

Fujun Lan: Writing – review & editing, Visualization, Validation, Formal analysis, Data curation. **Ziliang Yin:** Writing – original draft, Visualization, Methodology, Investigation, Formal analysis, Data curation, Conceptualization. **Hongbo Lou:** Writing – review & editing, Validation, Supervision, Formal analysis. **Xin Zhang:** Validation, Investigation, Formal analysis. **Lianghua Xiong:** Formal analysis, Data curation. **Di Peng:** Methodology, Investigation, Formal analysis, Data curation. **Dazhe Xu:** Formal analysis, Data curation. **Chenjie Lou:** Formal analysis, Data curation. **Tao Liang:** Investigation, Data curation. **Mingxue Tang:** Validation, Resources, Investigation. **Hongwei Sheng:** Writing – review & editing, Validation, Formal analysis. **Zhidan Zeng:** Writing – review & editing, Supervision, Resources, Project administration, Investigation. **Qiaoshi Zeng:** Writing – review & editing, Writing – original draft, Validation, Supervision, Resources, Project administration, Methodology, Investigation, Funding acquisition, Formal analysis, Conceptualization.

Declaration of competing interest

The authors declare that they have no known competing financial interests or personal relationships that could have appeared to influence the work reported in this paper.

Acknowledgments

This research was supported by Shanghai Science and Technology Committee (Grant No. 22JC1410300), and Shanghai Key Laboratory of Material Frontiers Research in Extreme Environments (Grant No.22dz2260800). We thank the Shanghai Synchrotron Radiation Facility of BL15U1(https://cstr.cn/31124.02.SSRF.BL15U1) for the assistance on XRD measurements. The Ce L_3-edge XAS experiments were performed at the beamline 13-IDE of GeoSoilEnviroCARS, Advanced Photon Source (APS), Argonne National Laboratory, USA. GeoSoilEnviroCARS was supported by the National Science Foundation-Earth Sciences (EAR-1634415). This research used resources of the Advanced Photon Source, a U.S. Department of Energy (DOE) Office of Science User Facility operated for the DOE Office of Science by Argonne National Laboratory under Contract No. DE-AC02-06CH11357.

Supplementary materials

Supplementary material associated with this article can be found, in the online version, at doi:10.1016/j.actamat.2026.122100.

References

[1] N.P. Armitage, P. Fournier, R.L. Greene, Progress and perspectives on electron-doped cuprates, Rev. Mod. Phys. 82 (2010) 2421–2487.
[2] A.L. Greer, E. Ma, Bulk metallic glasses: At the cutting edge of metals research, MRS Bull. 32 (2007) 611–619.
[3] A. Inoue, Stabilization of metallic supercooled liquid and bulk amorphous alloys, Acta Mater. 48 (2000) 279–306.
[4] C.J. Gilbert, R.O. Ritchie, W.L. Johnson, Fracture toughness and fatigue-crack propagation in a Zr–Ti–Ni–Cu–Be bulk metallic glass, Appl. Phys. Lett. 71 (1997) 476–478.
[5] A. Inoue, B. Shen, H. Koshiba, H. Kato, A.R. Yavari, Cobalt-based bulk glassy alloy with ultrahigh strength and soft magnetic properties, Nat. Mater. 2 (2003) 661–663.
[6] H. Ma, J. Xu, E. Ma, Mg-based bulk metallic glass composites with plasticity and high strength, Appl. Phys. Lett. 83 (2003) 2793–2795.
[7] D.C. Hofmann, J.-Y. Suh, A. Wiest, G. Duan, M.-L. Lind, M.D. Demetriou, W. L. Johnson, Designing metallic glass matrix composites with high toughness and tensile ductility, Nature 451 (2008) 1085–1089.
[8] J. Ma, X.Y. Zhang, D.P. Wang, D.Q. Zhao, D.W. Ding, K. Liu, W.H. Wang, Superhydrophobic metallic glass surface with superior mechanical stability and corrosion resistance, Appl. Phys. Lett. 104 (2014) 173701.
[9] S.V. Madge, A. Caron, R. Gralla, G. Wilde, S.K. Mishra, Novel W-based metallic glass with high hardness and wear resistance, Intermetallics 47 (2014) 6–10.
[10] W.H. Wang, Bulk metallic glasses with functional physical properties, Adv. Mater. 21 (2009) 4524–4544.
[11] W.H. Wang, The elastic properties, elastic models and elastic perspectives of metallic glasses, Prog. Mater. Sci. 57 (2012) 487–656.
[12] Y. Li, Q. Guo, J.A. Kalb, C.V. Thompson, Matching glass-forming ability with the density of the amorphous phase, Science 322 (2008) 1816–1819.
[13] J.H. Na, M.D. Demetriou, M. Floyd, A. Hoff, G.R. Garrett, W.L. Johnson, Compositional landscape for glass formation in metal alloys, Proc. Natl. Acad. Sci. 111 (2014) 9031–9036.
[14] H.W. Sheng, H.Z. Liu, Y.Q. Cheng, J. Wen, P.L. Lee, W.K. Luo, S.D. Shastri, E. Ma, Polyamorphism in a metallic glass, Nat. Mater. 6 (2007) 192–197.
[15] Q.S. Zeng, Y.C. Li, C.M. Feng, P. Liermann, M. Somayazulu, G.Y. Shen, H.K. Mao, R. Yang, J. Liu, T.D. Hu, J.Z. Jiang, Anomalous compression behavior in lanthanum/cerium-based metallic glass under high pressure, Proc. Natl. Acad. Sci. U.S.A. 104 (2007) 13565–13568.
[16] Q.S. Zeng, Y. Ding, W.L. Mao, W. Yang, S.V. Sinogeikin, J. Shu, H.K. Mao, J. Z. Jiang, Origin of pressure-induced polyamorphism in $Ce_{75}Al_{25}$ metallic glass, Phys. Rev. Lett. 104 (2010) 105702.
[17] Q.S. Zeng, Y.Z. Fang, H.B. Lou, Y. Gong, X.D. Wang, K. Yang, A.G. Li, S. Yan, C. Lathe, F.M. Wu, X.H. Yu, J.Z. Jiang, Low-density to high-density transition in Ce75Al23Si2 metallic glass, J. Phys. Condens. Matter. 22 (2010) 375404.
[18] M.J. Duarte, P. Bruna, E. Pineda, D. Crespo, G. Garbarino, R. Verbeni, K. Zhao, W. H. Wang, A.H. Romero, J. Serrano, Polyamorphic transitions in Ce-based metallic glasses by synchrotron radiation, Phys. Rev. B 84 (2011) 224116.
[19] G. Li, Y.Y. Wang, P.K. Liaw, Y.C. Li, R.P. Liu, Electronic structure inheritance and pressure-induced polyamorphism in lanthanide-based metallic glasses, Phys. Rev. Lett. 109 (2012) 125501.
[20] L. Li, Q. Luo, R. Li, H. Zhao, K.W. Chapman, P.J. Chupas, L. Wang, H. Liu, Polyamorphism in Yb-based metallic glass induced by pressure, Sci. Rep. 7 (2017) 46762.
[21] Z. Yin, H. Lou, H. Sheng, Z. Zeng, W.L. Mao, Q. Zeng, Polyamorphism in a solute-lean Al–Ce metallic glass, J. Appl. Phys. 129 (2021) 025108.
[22] H.B. Lou, Y.K. Fang, Q.S. Zeng, Y.H. Lu, X.D. Wang, Q.P. Cao, K. Yang, X.H. Yu, L. Zheng, Y.D. Zhao, W.S. Chu, T.D. Hu, Z.Y. Wu, R. Ahuja, J.Z. Jiang, Pressure-induced amorphous-to-amorphous configuration change in Ca-Al metallic glasses, Sci. Rep. 2 (2012) 376.
[23] Q. Du, X.-J. Liu, Q. Zeng, H. Fan, H. Wang, Y. Wu, S.-W. Chen, Z.-P. Lu, Polyamorphic transition in a transition metal based metallic glass under high pressure, Phys. Rev. B 99 (2019) 014208.
[24] Q. Zeng, H. Sheng, Y. Ding, L. Wang, W. Yang, J.Z. Jiang, W.L. Mao, H.K. Mao, Long-range topological order in metallic glass, Science 332 (2011) 1404–1406.
[25] Q. Zeng, W.L. Mao, H. Sheng, Z. Zeng, Q. Hu, Y. Meng, H. Lou, F. Peng, W. Yang, S.V. Sinogeikin, J.-Z. Jiang, The effect of composition on pressure-induced devitrification in metallic glasses, Appl. Phys. Lett. 102 (2013) 171905.
[26] M. Stolpe, I. Jonas, S. Wei, Z. Evenson, W. Hembree, F. Yang, A. Meyer, R. Busch, Structural changes during a liquid-liquid transition in the deeply undercooled $Zr_{58.5}Cu_{15.6}Ni_{12.8}Al_{10.3}Nb_{2.8}$ bulk metallic glass forming melt, Phys. Rev. B 93 (2016) 014201.
[27] W. Dmowski, S. Gierlotka, Z. Wang, Y. Yokoyama, B. Palosz, T. Egami, Pressure induced liquid-to-liquid transition in Zr-based supercooled melts and Pressure quenched glasses, Sci. Rep. 7 (2017) 6564.
[28] S. Hechler, B. Ruta, M. Stolpe, E. Pineda, Z. Evenson, O. Gross, A. Bernasconi, R. Busch, I. Gallino, Microscopic evidence of the connection between liquid-liquid transition and dynamical crossover in an ultraviscous metallic glass former, Phys. Rev. Mater. 2 (2018) 085603.
[29] S. Lan, Y. Ren, X.Y. Wei, B. Wang, E.P. Gilbert, T. Shibayama, S. Watanabe, M. Ohnuma, X.L. Wang, Hidden amorphous phase and reentrant supercooled liquid in Pd-Ni-P metallic glasses, Nat. Commun. 8 (2017) 14679.
[30] Q. Du, X. Liu, H. Fan, Q. Zeng, Y. Wu, H. Wang, D. Chatterjee, Y. Ren, Y. Ke, P. M. Voyles, Z. Lu, E. Ma, Reentrant glass transition leading to ultrastable metallic glass, Mater. Today 34 (2020) 66–77.
[31] H. Lou, Z. Zeng, F. Zhang, S. Chen, P. Luo, X. Chen, Y. Ren, V.B. Prakapenka, C. Prescher, X. Zuo, T. Li, J. Wen, W.H. Wang, H. Sheng, Q. Zeng, Two-way tuning of structural order in metallic glasses, Nat. Commun. 11 (2020) 314.
[32] J. Shen, Z. Lu, J.Q. Wang, S. Lan, F. Zhang, A. Hirata, M.W. Chen, X.L. Wang, P. Wen, Y.H. Sun, H.Y. Bai, W.H. Wang, Metallic glacial glass formation by a first-order liquid-liquid transition, J. Phys. Chem. Lett. 11 (2020) 6718–6723.
[33] J. Shen, Y.H. Sun, J. Orava, H.Y. Bai, W.H. Wang, Liquid-to-liquid transition around the glass-transition temperature in a glass-forming metallic liquid, Acta Mater. 225 (2022) 117588.
[34] Q. Yang, X.-M. Yang, T. Zhang, X.-W. Liu, H.-B. Yu, Structure and entropy control of polyamorphous transition in high-entropy metallic glasses, Acta Mater. 266 (2024) 119701.
[35] J. Schroers, Bulk metallic glasses, Phys. Today 66 (2013) 32–37.
[36] C. Tang, W. Pan, B. Zhang, J. Wang, H. Zhou, Investigation of glass forming ability in Ce–Al–Co (Cu) alloys, J. Non-Cryst. Solids 383 (2014) 6–12.
[37] C. Prescher, V.B. Prakapenka, DIOPTAS: a program for reduction of two-dimensional X-ray diffraction data and data exploration, High Press. Res. 35 (2015) 223–230.
[38] W.C. Oliver, G.M. Pharr, Measurement of hardness and elastic modulus by instrumented indentation: advances in understanding and refinements to methodology, J. Mater. Res. 19 (2004) 3–20.
[39] H.E. Kissinger, Reaction kinetics in differential thermal analysis, Anal. Chem. 29 (1957) 1702–1706.
[40] T. Ozawa, Kinetic analysis of derivative curves in thermal analysis, J. Therm. Anal. 2 (1970) 301–324.
[41] R. Böhmer, K.L. Ngai, C.A. Angell, D.J. Plazek, Nonexponential relaxations in strong and fragile glass formers, J. Chem. Phys. 99 (1993) 4201–4209.
[42] C. Yuan, R. Liu, Z. Lv, X. Li, C. Pang, C. Yang, J. Ma, W. Wang, Softening in an ultrasonic-vibrated Pd-based metallic glass, Intermetallics 144 (2022) 107527.
[43] F. Jin, C.M. Pang, X.M. Wang, C.C. Yuan, The role of rare earth elements in tailorable thermal and magnetocaloric properties of RE-Co-Al (RE = Gd, Tb, and Dy) metallic glasses, J. Non-Cryst. Solids 600 (2023).
[44] C.A. Angell, Formation of glasses from liquids and biopolymers, Science 267 (1995) 1924–1935.
[45] W.J. Wright, R. Saha, W.D. Nix, Deformation mechanisms of the $Zr_{40}Ti_{14}Ni_{10}Cu_{12}Be_{24}$ bulk metallic glass, Mater. Trans. JIM 42 (2001) 642–649.
[46] C.A. Schuh, T.G. Nieh, Y. Kawamura, Rate dependence of serrated flow during nanoindentation of a bulk metallic glass, J. Mater. Res. 17 (2002) 1651–1654.
[47] C.A. Schuh, T.G. Nieh, A nanoindentation study of serrated flow in bulk metallic glasses, Acta Mater. 51 (2003) 87–99.
[48] B.A. Sun, H.B. Yu, W. Jiao, H.Y. Bai, D.Q. Zhao, W.H. Wang, Plasticity of ductile metallic glasses: a self-organized critical state, Phys. Rev. Lett. 105 (2010) 035501.
[49] D. Klaumunzer, A. Lazarev, R. Maass, F.H. Dalla Torre, A. Vinogradov, J. F. Loffler, Probing shear-band initiation in metallic glasses, Phys. Rev. Lett. 107 (2011) 185502.
[50] G. Liao, Z. Long, M. Zhao, M. Zhong, W. Liu, W. Chai, Serrated flow behavior in a Pd-based bulk metallic glass under nanoindentation, J. Non-Cryst. Solids 460 (2017) 47–53.
[51] G.K. Liao, Z.L. Long, M.S.Z. Zhao, L. Peng, W. Chai, Z.H. Ping, Nanoindentation study on the characteristic of shear transformation zone in a Pd-based bulk metallic glass during serrated flow, Phys. B: Condens. Matter. 534 (2018) 163–168.
[52] K.F. Kelton, F. Spaepen, Kinetics of structural relaxation in several metallic glasses observed by changes in electrical resistivity, Phys. Rev. B 30 (1984) 5516–5524.
[53] O. Haruyama, N. Annoshita, H. Kimura, N. Nishiyama, A. Inoue, Anomalous behavior of electrical resistivity in glass transition region of a bulk Pd40Ni40P20 metallic glass, J. Non-Cryst. Solids 312-314 (2002) 552–556.
[54] J. Guo, F. Zu, Z. Chen, S. Zheng, Y. Yuan, Exploration of a new method in determining the glass transition temperature of BMGs by electrical resistivity, Solid State Commun 135 (2005) 103–107.
[55] I.A. Yakubtsov, Effects of composition and microstructure on behaviors of electrical resistivity during continuous heating above room temperature in Mg-based alloys, J. Alloys Compd. 492 (2010) 153–159.
[56] H.W. Yang, J. Gong, R.D. Li, J.Q. Wang, Thermal variation of electrical resistance of an $Al_{85}Ni_5Y_8Co_2$ metallic glass free of quenched-in nuclei, J. Non-Cryst. Solids 355 (2009) 2205–2208.
[57] U. Mizutani, M. Sasaura, Y. Yamada, T. Matsuda, Electronic structure and electron transport of Ca-Mg-Al metallic glasses, J. Phys. F: Met. Phys. 17 (1987) 667–678.
[58] M.A. Howson, Incipient localisation and electron-electron correlation effects in metallic glass alloys, J. Phys. F: Met. Phys. 14 (1984) L25–L31.
[59] N.F. Mott, Conduction in non-crystalline materials, Philos. Mag. 19 (1969) 835–852.
[60] J. Antonowicz, A. Pietnoczka, K. Pękała, J. Latuch, G.A. Evangelakis, Local atomic order, electronic structure and electron transport properties of Cu-Zr metallic glasses, J. Appl. Phys. 115 (2014) 203714.
[61] M. Brian Maple, Strongly correlated electron phenomena in f-electron materials, J. Phys. Soc. Jpn. 74 (2005) 222–238.

[62] Q.S. Zeng, C.R. Rotundu, W.L. Mao, J.H. Dai, Y.M. Xiao, P. Chow, X.J. Chen, C. L. Qin, H.k. Mao, J.Z. Jiang, Low temperature transport properties of Ce-Al metallic glasses, J. Appl. Phys. 109 (2011) 113716.
[63] D. Malterre, G. Krill, J. Durand, G. Marchal, M.F. Ravet, Electronic configuration of cerium in amorphous alloys investigated by x-ray absorption spectroscopy, Phys. Rev. B 34 (1986) 2176–2181.
[64] J.P. Rueff, J.P. Itie, M. Taguchi, C.F. Hague, J.M. Mariot, R. Delaunay, J. P. Kappler, N. Jaouen, Probing the transition in bulk Ce under pressure: a direct investigation by resonant inelastic X-ray scattering, Phys. Rev. Lett. 96 (2006) 237403.
[65] R.A. Neifeld, M. Croft, T. Mihalisin, C.U. Segre, M. Madigan, M.S. Torikachvili, M. B. Maple, L.E. DeLong, Chemical environment and Ce valence: global trends in transition-metal compounds, Phys. Rev. B 32 (1985) 6928–6931.
[66] M. Münzenberg, W. Felsch, P. Schaaf, Tuning the 4*f* state occupancy of Ce in highly correlated CeSi/Fe multilayers: an x-ray absorption spectroscopy study, Phys. Rev. B 76 (2007) 014427.
[67] D. Gignoux, F. Givord, R. Lemaire, H. Launois, F. Sayetat, Valence state of cerium in the hexagonal CeM5 compounds with the transition metals, J. Phys. 43 (1982) 173–180.
[68] J.W. Allen, R.M. Martin, Kondo volume collapse and the γ→α transition in cerium, Phys. Rev. Lett. 49 (1982) 1106.
[69] O. Eriksson, R.C. Albers, A.M. Boring, G.W. Fernando, Y.G. Hao, B.R. Cooper, Surface electronic structure of Ce in the α and γ phase, Phys. Rev. B 43 (1991) 3137–3142.
[70] W. Felsch, S.G. Kushnir, K. Samwer, H. Schröder, R. van den Berg, Delocalization of the Ce 4*f* shell in amorphous $Ce_{75.5}Co_{24.5}$, Z. Phys. B: Condens. Matter. 48 (1982) 99–107.
[71] W. Felsch, S.G. Kushnir, K. Samwer, Crystal-field effects and magnetic interactions in amorphous Ce89Al11, J. Phys. Colloq. 41 (1980) C8–630.
[72] V.A. Polukhin, E.D. Kurbanova, N.A. Vatolin, Formation of a intermediate order in metallic glasses and a long order in nanocrystalline alloys with allowance for the character of binding and the transformation of the short order in a melt, Russ. Metall. 2018 (2018) 95–109.
[73] P.F. Guan, T. Fujita, A. Hirata, Y.H. Liu, M.W. Chen, Structural origins of the excellent glass forming ability of $Pd_{40}Ni_{40}P_{20}$, Phys. Rev. Lett. 108 (2012) 175501.
[74] A.N. Mansour, C. Wong, R.A. Brizzolara, Atomic structure of amorphous $Al_{100-2x}Co_xCe_x$ (x = 8, 9, and 10) and $Al_{80}Fe_{10}Ce_{10}$ alloys: an XAFS study, Phys. Rev. B 50 (1994) 12401–12412.
[75] B. Zhang, R.J. Wang, W.H. Wang, Response of acoustic and elastic properties to pressure and crystallization of Ce-based bulk metallic glass, Phys. Rev. B 72 (2005) 104205.
[76] J. Kim, H.S. Oh, J. Kim, C.W. Ryu, G.W. Lee, H.J. Chang, E.S. Park, Utilization of high entropy alloy characteristics in Er-Gd-Y-Al-Co high entropy bulk metallic glass, Acta Mater. 155 (2018) 350–361.
[77] T. Rouxel, Y. Yokoyama, Elastic properties and atomic bonding character in metallic glasses, J. Appl. Phys. 118 (2015) 044901.
[78] L. Tichý, H. Tichá, Covalent bond approach to the glass-transition temperature of chalcogenide glasses, J. Non-Cryst. Solids 189 (1995) 141–146.
[79] X.J. Gu, S.J. Poon, G.J. Shiflet, M. Widom, Mechanical properties, glass transition temperature, and bond enthalpy trends of high metalloid Fe-based bulk metallic glasses, Appl. Phys. Lett. 92 (2008) 161910.
[80] L. Zhang, Y.-Q. Cheng, A.J. Cao, J. Xu, E. Ma, Bulk metallic glasses with large plasticity: composition design from the structural perspective, Acta Mater. 57 (2009) 1154–1164.
[81] F. Moitzi, D. Şopu, D. Holec, D. Perera, N. Mousseau, J. Eckert, Chemical bonding effects on the brittle-to-ductile transition in metallic glasses, Acta Mater. 188 (2020) 273–281.
[82] A. Takeuchi, A. Inoue, Classification of bulk metallic glasses by atomic size difference, heat of mixing and period of constituent elements and its application to characterization of the main alloying element, Mater. Trans. JIM 46 (2005) 2817–2829.
[83] L. Lai, T. Liu, X. Cai, M. Wang, S. Zhang, W. Chen, S. Guo, High-temperature Mo-based bulk metallic glasses, Scr. Mater. 203 (2021) 114095.
[84] X. Zhang, L. Lai, S. Xiao, H. Zhang, F. Zhang, N. Li, S. Guo, Effect of W on the thermal stability, mechanical properties and corrosion resistance of Fe-based bulk metallic glass, Intermetallics 143 (2022) 107485.
[85] T. Takeuchi, D. Fukamaki, H. Miyazaki, K. Soda, M. Hasegawa, H. Sato, U. Mizutani, T. Ito, S. Kimura, Electronic structure and stability of the Pd-Ni-P bulk metallic glass, Mater. Trans. JIM 48 (2007) 1292–1298.
[86] D.V. Louzguine-Luzgin, R. Belosludov, A.R. Yavari, K. Georgarakis, G. Vaughan, Y. Kawazoe, T. Egami, A. Inoue, Structural basis for supercooled liquid fragility established by synchrotron-radiation method and computer simulation, J. Appl. Phys. 110 (2011) 043519.
[87] J. Durand, P. Panissod, NMR in metallic glasses, J. Magn. Magn. Mater. 31-34 (1983) 1567–1570.
[88] X.K. Xi, L.L. Li, B. Zhang, W.H. Wang, Y. Wu, Correlation of atomic cluster symmetry and glass-forming ability of metallic glass, Phys. Rev. Lett. 99 (2007) 095501.
[89] X.K. Xi, M.T. Sandor, H.J. Wang, J.Q. Wang, W.H. Wang, Y. Wu, Bonding characters of Al-containing bulk metallic glasses studied by 27Al NMR, J. Phys. Condens. Matter. 23 (2011) 115501.
[90] C.C. Yuan, J.F. Xiang, X.K. Xi, W.H. Wang, NMR signature of evolution of ductile-to-brittle transition in bulk metallic glasses, Phys. Rev. Lett. 107 (2011) 236403.
[91] C.C. Yuan, Y.F. Yang, X.K. Xi, Atomic and electronic structure of Ni-Nb metallic glasses, J. Appl. Phys. 114 (2013) 213511.
[92] C.C. Yuan, F. Yang, X.K. Xi, C.L. Shi, D. Holland-Moritz, M.Z. Li, F. Hu, B.L. Shen, X.L. Wang, A. Meyer, W.H. Wang, Impact of hybridization on metallic-glass formation and design, Mater. Today 32 (2020) 26–34.
[93] M. Wencka, M. Bobnar, T. Apih, Q. Hu, S. Guo, J. Dolinšek, Al^{27} NMR local study of the $Al_{0.5}TiZrPdCuNi$ alloy in high-entropy alloy and metallic glass forms, Phys. Rev. B 105 (2022) 174208.
[94] Y. Wang, X. Zhang, J. Qiang, Q. Wang, D. Wang, D. Li, C.H. Shek, C. Dong, Composition optimization of the Al–Co–Zr bulk metallic glasses, Scr. Mater. 50 (2004) 829–833.
[95] C.C. Yuan, X. Shen, J. Cui, L. Gu, R.C. Yu, X.K. Xi, Atomic and electronic structures of Zr-(Co,Ni,Cu)-Al metallic glasses, Appl. Phys. Lett. 101 (2012) 021902.
[96] S.A. Uporov, V.A. Bykov, D.A. Yagodin, Thermophysical properties of the $Al_{83}Co_{10}Ce_7$ glass-forming alloy in crystalline and liquid states, J. Alloys Compd. 589 (2014) 420–424.
[97] C.C. Yuan, F. Yang, F. Kargl, D. Holland-Moritz, G.G. Simeoni, A. Meyer, Atomic dynamics in Zr-(Co,Ni)-Al metallic glass-forming liquids, Phys. Rev. B 91 (2015) 214203.
[98] N.C. Wu, L. Zuo, J.Q. Wang, E. Ma, Designing aluminum-rich bulk metallic glasses via electronic-structure-guided microalloying, Acta Mater. 108 (2016) 143–151.
[99] K. Han, J. Qiang, Y. Wang, P. Häussler, Zr-Al-Co-Cu bulk metallic glasses for biomedical devices applications, J. Alloys Compd. 729 (2017) 144–149.
[100] G. Yang, J. Lian, R. Wang, N. Wu, Similar atom substitution effect on the glass forming ability in (La Ce) Al-(Ni Co) bulk metallic glasses using electron structure guiding, J. Alloys Compd. 786 (2019) 250–256.